

Dynamic Modeling of a Skid-Steered Wheeled Vehicle with Experimental Verification

Wei Yu, Oscar Chuy Jr., Emmanuel G. Collins Jr., and Patrick Hollis

Abstract—Skid-steered vehicles are often used as outdoor mobile robots due to their robust mechanical structure and high maneuverability. Sliding along with rolling is inherent to general curvilinear motion, which makes both kinematic and dynamic modeling difficult. For the purpose of motion planning this paper develops and experimentally verifies dynamic models of a skid-steered wheeled vehicle for general planar (2D) motion and for linear 3D motion. These models are characterized by the coefficient of rolling resistance, the coefficient of friction, and the shear deformation modulus, which have terrain-dependent values. The dynamic models also include motor saturation and motor power limitations, which enable correct prediction of vehicle velocities when traversing hills. It is shown that the closed-loop system that results from inclusion of the dynamics of the (PID) speed controllers for each set of wheels does a much better job than the open loop model of predicting the vehicle linear and angular velocities. Hence, the closed-loop model is recommended for motion planning.

I. INTRODUCTION

Dynamic models of autonomous ground vehicles are needed to enable realistic motion predictions in unstructured, outdoor environments that have substantial changes in elevation, consist of a variety of terrain surfaces, and/or require frequent accelerations and decelerations. At least 4 different planning tasks can be accomplished using appropriate dynamic models: 1) time optimal motion planning, 2) energy efficient motion planning, 3) planning in the presence of a fault, 4) reduction in the frequency of replanning.

Ackerman steering, differential steering, and skid steering are the most widely applied steering mechanisms for wheeled and tracked vehicles. Ackerman steering has the advantage of good controllability [1], but has the disadvantages of low maneuverability and a complex steering subsystem [2]. Differential steering is popular because it provides high maneuverability with a zero turning radius and has a simple steering configuration [1]. However, it has limited mobility on outdoor terrains. Like differential steering, skid steering leads to high maneuverability [1], [3] and also has a simple and robust mechanical structure [4], [5]. In contrast, it has good mobility on a variety of terrains, which makes it suitable for all-terrain traversal.

A skid-steered vehicle can be characterized by two features [1], [2]. First, the vehicle steering depends on controlling the relative velocities of the left and right side wheels. Second, all wheels or tracks point to the longitudinal axis

of the vehicle and vehicle turning requires slippage of the wheels or tracks. Due to identical steering mechanisms, wheeled and tracked skid-steered vehicles share many properties [2], [5], [6], [7]. Many of the difficulties associated with modeling and operating both classes of skid-steered vehicles arise from the complex wheel (or track) and terrain interaction [2], [7]. For Ackerman-steered or differential-steered vehicles, the wheel motions may often be accurately modeled by pure rolling, while for skid-steered vehicles in general curvilinear motion, the wheels (or tracks) roll and slide at the same time [2], [5], [7], [8]. This makes it difficult to develop kinematic and dynamic models that accurately describe the motion. Other disadvantages are that the motion tends to be energy inefficient, difficult to control [4], [9], and for wheeled vehicles, the tires tend to wear out faster.

A kinematic model of a skid-steered wheeled vehicle maps the wheel velocities to the vehicle velocities and is an important component in the development of a dynamic model. In contrast to the kinematic models for Ackerman-steered and differentially-steered vehicles, the kinematic model of a skid-steered vehicle is terrain-dependent [2], [10] and is dependent on more than the physical dimensions of the vehicle. In [2], [9] a kinematic model of a skid-steered vehicle was developed by assuming a certain equivalence with a kinematic model of a differential-steered vehicle. This was accomplished by experimentally determining the instantaneous centers of rotation (ICRs) of the sliding velocities of the left and right wheels. An alternative kinematic model that is based on the slip ratios of the wheels has been presented in [6], [10]. This model takes into account the longitudinal slip ratios of the left and right wheels. The difficulty in using this model is the actual detection of slip, which cannot be computed analytically. Hence, developing practical methods to experimentally determine the slip ratios is an active research area [5], [6].

To date, there is very little published research on the experimentally verified dynamic models for general motion of skid-steered vehicles, especially wheeled vehicles. The main reason is that it is hard to model the tire (or track) and terrain interaction when slipping and skidding occur. (For each vehicle wheel, if the wheel velocity computed using the angular velocity of the wheel is larger than the actual linear velocity of the wheel, slipping occurs, while if the computed wheel velocity is smaller than the actual linear velocity, skidding occurs.) The research of [3] developed a dynamic model for planar motion by considering longitudinal rolling resistance, lateral friction, moment of resistance for the vehicle, and also the nonholonomic constraint for lateral

W. Yu, O. Chuy, E. Collins, and P. Hollis are with the Center for Intelligent Systems, Control and Robotics (CISCOR) and the Department of Mechanical Engineering, Florida A&M University-Florida State University, Tallahassee, FL 32310, USA {yuwei, chuy, ecollins, hollis}@eng.fsu.edu

skidding. In addition, a model-based nonlinear controller was designed for trajectory tracking. However, this model uses Coulomb friction to describe the lateral sliding friction and moment of resistance, which contradicts empirical evidence [10], [11]. In addition, it does not consider any of the motor properties. Furthermore, the results of [3] are limited to simulation without experimental verification.

The research of [4] developed a planar dynamic model of a skid-steered vehicle, which is essentially that of [3], using a different velocity vector (consisting of the longitudinal and angular velocities of the vehicle instead of the longitudinal and lateral velocities). In addition, the dynamics of the motors, though not the power limitations, were added to the model. Kinematic, dynamic and motor level control laws were explored for trajectory tracking. However, as in [3], Coulomb friction was used to describe the lateral friction and moment of resistance, and the results are limited to simulation.

The most thorough dynamic analysis of a skid-steered vehicle is found in [10], [11], which consider steady-state (i.e., constant linear and angular velocities) dynamic models for circular motion of *tracked* vehicles. A primary contribution of this research is that it proposes and then provides experimental evidence that in the track-terrain interaction the shear stress is a particular function of the shear displacement (see eqn. (7) of Section III). This model differs from the Coulomb model of friction, adopted in [3], [4], which essentially assumes that the maximum shear stress is obtained as soon as there is any relative movement between the track and the ground. This research also provides detailed analysis of the longitudinal and lateral forces that act on a tracked vehicle. But their results had not been extended to skid-steered *wheeled* vehicles. In addition, they do not consider vehicle acceleration, terrain elevation, actuator limitations, or the vehicle control system.

Building upon the research in [10], [11], this paper develops dynamic models of a skid-steered wheeled vehicle for general curvilinear planar (2D) motion and straight-line 3D motion. As in [10], [11] the modeling is based upon the functional relationship of shear stress to shear displacement. Practically, this means that for a vehicle tire the shear stress varies with the turning radius. This research also includes models of the saturation and power limitations of the actuators as part of the overall vehicle model. In addition, it shows that the closed-loop model yields substantially better predictions of the vehicle velocity than the corresponding open-loop model.

The paper is organized as follows. Section II describes the terrain-dependent kinematic model needed for the development of the dynamic model. Section III discusses the wheel and terrain interaction of a skid-steered wheeled vehicle and establishes the dynamic models. Section IV describes the closed-loop model, including the discussion of the PID controller, motor and motor controller. Section V experimentally verifies the dynamic models in planar and hill-climbing experiments. Finally, Section VI concludes the paper and discusses future research.

II. KINEMATIC MODELS

In this section, the kinematic model of a skid-steered wheeled vehicle is described and discussed. It is an important component in the development of the overall dynamic model of a skid-steered vehicle.

To mathematically describe the kinematic models that have been developed for skid-steered vehicles, consider a wheeled vehicle moving at constant velocity about an instantaneous center of rotation (see Fig. 1 of Section III). The local coordinate frame, attached to the body center of gravity, is denoted by x - y , where x is the lateral coordinate and y is the longitudinal coordinate.

For vehicles that are symmetric about the x and y axes, an experimental kinematic model of a skid-steered wheeled vehicle that is developed in [2] is given by,

$$\begin{bmatrix} v_y \\ \dot{\varphi} \end{bmatrix} = \frac{r}{\alpha B} \begin{bmatrix} \frac{\alpha B}{2} & \frac{\alpha B}{2} \\ -1 & 1 \end{bmatrix} \begin{bmatrix} \omega_l \\ \omega_r \end{bmatrix}, \quad (1)$$

where ω_l and ω_r are respectively the angular velocities of the left and right wheels, v_y is the vehicle velocity in the longitudinal direction, $\dot{\varphi}$ is the vehicle angular velocity, B is the vehicle width, r is the wheel radius, and α is a terrain-dependent parameter that is a function of the ICRs. (Note that the lateral velocity $v_x = 0$.) Our experimental results show that the larger the rolling resistance, the larger the value of α . For a Pioneer 3-AT mobile robot (see Fig. 4 of Section V), $\alpha = 1.5$ for a vinyl lab surface and $\alpha > 2$ for a concrete surface. (More experiments are needed to obtain the precise α for a concrete surface.) Equation (1) shows that the kinematic model of a skid-steered wheeled vehicle of width B is equivalent to the kinematic model of a differential-steered wheeled vehicle of width αB .

A more rigorously derived kinematic model for a skid-steered vehicle is presented in [6], [10]. This model takes into account the longitudinal slip ratios i_l and i_r of the left and right wheels and for symmetric vehicles is given by

$$\begin{bmatrix} v_y \\ \dot{\varphi} \end{bmatrix} = \frac{r}{B} \begin{bmatrix} \frac{(1-i_l)B}{2} & \frac{(1-i_r)B}{2} \\ -(1-i_l) & (1-i_r) \end{bmatrix} \begin{bmatrix} \omega_l \\ \omega_r \end{bmatrix}, \quad (2)$$

where $i_l \triangleq (r\omega_l - v_{l,a})/(r\omega_l)$, $i_r \triangleq (r\omega_r - v_{r,a})/(r\omega_r)$ and $v_{l,a}$ and $v_{r,a}$ are the actual velocities of the left and right wheels. We have found that when

$$\frac{i_l}{i_r} = -\frac{\omega_r}{\omega_l} \quad \text{and} \quad \alpha = \frac{1}{1 - \frac{2i_l i_r}{i_l + i_r}}, \quad (3)$$

(1) and (2) are identical. Currently, to our knowledge no analysis or experiments have been performed to verify the left hand equation in (3) and analyze its physical significance.

III. DYNAMIC MODELS

This section develops dynamic models of a skid-steered, wheeled vehicle for the cases of circular 2D motion and linear 3D motion. In contrast to dynamic models described in terms of the velocity vector of the vehicle [3], [4], the dynamic models here are described in terms of the angular velocity vector of the wheels. This is because the wheel (specifically, the motor) velocities are actually commanded

by the control system, so this model form is particularly beneficial for control and planning.

Following [4], the dynamic model considering the non-holonomic constraint is given by

$$M\ddot{q} + C(q, \dot{q}) + G(q) = \tau, \quad (4)$$

where $q = [\theta_l \ \theta_r]^T$ is the angular displacement of the left and right wheels, $\dot{q} = [\omega_l \ \omega_r]^T$ is the angular velocity of the left and right wheels, $\tau = [\tau_l \ \tau_r]^T$ is the torque of the left and right motors, M is the mass matrix, $C(q, \dot{q})$ is the resistance term, and $G(q)$ is the gravitational term.

A. 2D General Motion

When the vehicle is moving on a 2D surface, it follows from the model given in [4], which is expressed in the local x - y coordinates, and the kinematic model (1) that $M(q)$ in (4) is given by

$$M = \begin{bmatrix} \frac{mr^2}{4} + \frac{r^2 I}{\alpha B^2} & \frac{mr^2}{4} - \frac{r^2 I}{\alpha B^2} \\ \frac{mr^2}{4} - \frac{r^2 I}{\alpha B^2} & \frac{mr^2}{4} + \frac{r^2 I}{\alpha B^2} \end{bmatrix}, \quad (5)$$

where m and I are respectively the mass and moment of inertia of the vehicle. Since we are considering planar motion, $G(q) = 0$. $C(q, \dot{q})$ represents the resistance resulting from the interaction of the wheels and terrain, including the rolling resistance, sliding frictions, and the moment of resistance, the latter two of which are modeled using Coulomb friction in [3], [4]. Assume that $\dot{q} = [\omega_l \ \omega_r]^T$ is a known constant, then $\ddot{q} = 0$ and (4) becomes

$$C(q, \dot{q}) = \tau. \quad (6)$$

Based on the theory in [10], [11], the shear stress τ_{ss} and shear displacement j relationship can be described as,

$$\tau_{ss} = p\mu(1 - e^{-j/K}), \quad (7)$$

where p is the normal pressure, μ is the coefficient of friction and K is the shear deformation modulus. K is a terrain-dependent parameter, like the rolling resistance and coefficient of friction [10].

Fig. 1 depicts a skid-steered wheeled vehicle moving counterclockwise (CCW) at constant linear velocity v and angular velocity $\dot{\varphi}$ in a circle centered at O from position 1 to position 2. X - Y denotes the global frame and the body-fixed frames for the right and left wheels are given respectively by the x_r - y_r and x_l - y_l . The four contact patches of the wheels with the ground are shadowed in Fig. 1 and L and C are the patch-related distances shown in Fig. 1. It is assumed that the vehicle is symmetric and the center of gravity (CG) is at the geometric center. Note that because ω_l and ω_r are known, v_y and $\dot{\varphi}$ can be computed using the vehicle kinematic model (1), which enables the determination of the radius of curvature R since $v_y = R\dot{\varphi}$.

In the x_r - y_r frame consider an arbitrary point on the contact patch of the front right wheel with coordinates (x_{fr}, y_{fr}) . This contact patch is *not* fixed on the tire, but is the part of the tire that contacts the ground. The time

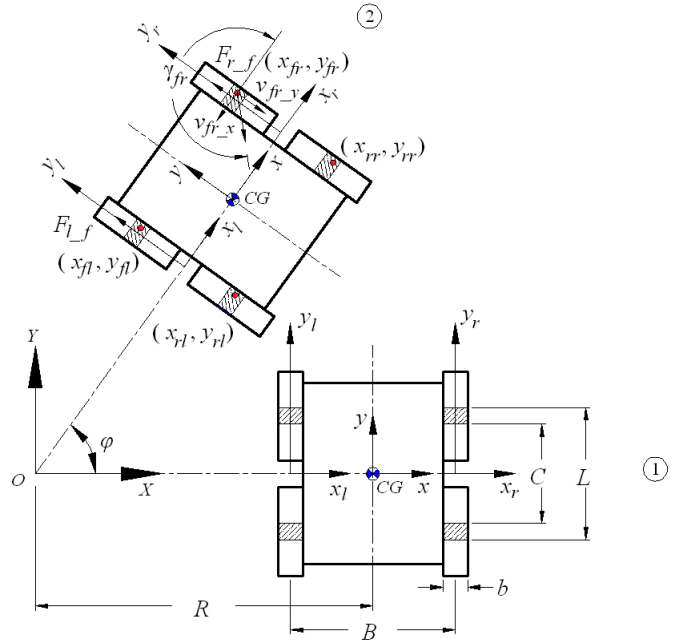


Fig. 1. Circular motion of a skid-steered wheeled vehicle interval t for this point to travel from an initial contact point $(x_{fr}, L/2)$ to (x_{fr}, y_{fr}) is,

$$t = \int_{y_{fr}}^{L/2} \frac{1}{r\omega_r} dy_r = \frac{L/2 - y_{fr}}{r\omega_r}. \quad (8)$$

During the same time, the vehicle has moved from position 1 to position 2 with an angular displacement of φ . The sliding velocities of point (x_{fr}, y_{fr}) in the x_r and y_r directions are denoted by v_{fr-x} and v_{fr-y} . Therefore,

$$v_{fr-x} = -y_{fr}\dot{\varphi}, \quad v_{fr-y} = (R + B/2 + x_{fr})\dot{\varphi} - r\omega_r. \quad (9)$$

The resultant sliding velocity v_{fr} and its angle γ_{fr} in the x_r - y_r frame are

$$v_{fr} = \sqrt{v_{fr-x}^2 + v_{fr-y}^2}, \quad \gamma_{fr} = \pi + \arctan\left(\frac{v_{fr-y}}{v_{fr-x}}\right). \quad (10)$$

Note that when the wheel is sliding, the direction of friction is opposite to the sliding velocity, and if the vehicle is in pure rolling, v_{fr-x} and v_{fr-y} are zero.

In order to calculate the shear displacement of this reference point, the sliding velocities need to be expressed in the global X - Y frame. Let v_{fr-X} and v_{fr-Y} denote the sliding velocities in the X and Y directions. Then, the transformation between the local and global sliding velocities is given by,

$$\begin{bmatrix} v_{fr-X} \\ v_{fr-Y} \end{bmatrix} = \begin{bmatrix} \cos \varphi & -\sin \varphi \\ \sin \varphi & \cos \varphi \end{bmatrix} \begin{bmatrix} v_{fr-x} \\ v_{fr-y} \end{bmatrix}. \quad (11)$$

The shear displacements j_{fr-X} and j_{fr-Y} in the X and Y directions can be expressed as

$$\begin{aligned} j_{fr-X} &= \int_0^t v_{fr-X} dt = \int_{y_{fr}}^{L/2} (v_{fr-x} \cos \varphi - v_{fr-y} \sin \varphi) \frac{1}{r\omega_r} dy_r \\ &= (R + B/2 + x_{fr}) \cdot \left\{ \cos\left[\frac{(L/2 - y_{fr})\dot{\varphi}}{r\omega_r}\right] - 1 \right\} \\ &\quad - y_{fr} \sin\left[\frac{(L/2 - y_{fr})\dot{\varphi}}{r\omega_r}\right], \end{aligned} \quad (12)$$

$$\begin{aligned}
j_{fr.Y} &= \int_0^t v_{fr.Y} dt = \int_{y_{fr}}^{L/2} (v_{fr.x} \sin \varphi + v_{fr.y} \cos \varphi) \frac{1}{r\omega_r} dy_r \\
&= (R + B/2 + x_{fr}) \cdot \sin\left[\frac{(L/2 - y_{fr})\dot{\varphi}}{r\omega_r}\right] - L/2 \\
&\quad + y_{fr} \cos\left[\frac{(L/2 - y_{fr})\dot{\varphi}}{r\omega_r}\right]. \quad (13)
\end{aligned}$$

$$\begin{aligned}
F_{l.f} &= \int_{C/2}^{L/2} \int_{-b/2}^{b/2} p_l \mu_l (1 - e^{-j_{fl}/K_l}) \sin(\pi + \gamma_{fl}) dx_l dy_l \\
&\quad + \int_{-L/2}^{-C/2} \int_{-b/2}^{b/2} p_l \mu_l (1 - e^{-j_{rl}/K_l}) \sin(\pi + \gamma_{rl}) dx_l dy_l, \quad (20)
\end{aligned}$$

The resultant shear displacement j_{fr} in the X - Y frame is given by $j_{fr} = \sqrt{j_{fr.X}^2 + j_{fr.Y}^2}$. Similarly, it can be shown that for the reference point (x_{rr}, y_{rr}) in the rear right wheel the angle of the sliding velocity γ_{rr} in the x_r - y_r frame is

$$\gamma_{rr} = \arctan\left[\frac{(R + B/2 + x_{rr})\dot{\varphi} - r\omega_r}{-y_{rr}\dot{\varphi}}\right], \quad (14)$$

and the shear displacements $j_{rr.X}$ and $j_{rr.Y}$ are given by

$$\begin{aligned}
j_{rr.X} &= (R + B/2 + x_{rr}) \cdot \left\{ \cos\left[\frac{(-C/2 - y_{rr})\dot{\varphi}}{r\omega_r}\right] - 1 \right\} \\
&\quad - y_{rr} \sin\left[\frac{(-C/2 - y_{rr})\dot{\varphi}}{r\omega_r}\right], \quad (15)
\end{aligned}$$

$$\begin{aligned}
j_{rr.Y} &= (R + B/2 + x_{rr}) \cdot \sin\left[\frac{(-C/2 - y_{rr})\dot{\varphi}}{r\omega_r}\right] + C/2 \\
&\quad + y_{rr} \cos\left[\frac{(-C/2 - y_{rr})\dot{\varphi}}{r\omega_r}\right]. \quad (16)
\end{aligned}$$

and the magnitude of the resultant shear displacement j_{rr} is $j_{rr} = \sqrt{j_{rr.X}^2 + j_{rr.Y}^2}$.

The friction force points in the opposite direction of the sliding velocity. Using j_{fr} and j_{rr} , derived above, with (7) and integrating along the contact patches yields that the longitudinal sliding friction of the right wheels $F_{r.f}$ can be expressed as

$$\begin{aligned}
F_{r.f} &= \int_{C/2}^{L/2} \int_{-b/2}^{b/2} p_r \mu_r (1 - e^{-j_{fr}/K_r}) \sin(\pi + \gamma_{fr}) dx_r dy_r \\
&\quad + \int_{-L/2}^{-C/2} \int_{-b/2}^{b/2} p_r \mu_r (1 - e^{-j_{rr}/K_r}) \sin(\pi + \gamma_{rr}) dx_r dy_r, \quad (17)
\end{aligned}$$

where p_r , μ_r and K_r are respectively the normal pressure, coefficient of friction, and shear deformation modulus of the right wheels.

Let $f_{r.r}$ denote the rolling resistance of the right wheels, including the internal locomotion resistance such as resistance from belts, motor windings and gearboxes [12]. The complete resistance torque $\tau_{r.Res}$ from the ground to the right wheel is given by

$$\tau_{r.Res} = r(F_{r.f} + f_{r.r}). \quad (18)$$

Since ω_r is constant, the input torque τ_r from right motor will compensate for the resistance torque, such that

$$\tau_r = \tau_{r.Res}. \quad (19)$$

The above discussion is for the right wheel. Exploiting the same derivation process, one can obtain analytical expressions for the shear displacements j_{fl} and j_{rl} of the front and rear left wheels, and the angles of the sliding velocity γ_{fl} and γ_{rl} . The longitudinal sliding friction of the left wheels $F_{l.f}$ is then given by

where p_l , μ_l and K_l are respectively the normal pressure, coefficient of friction, and shear deformation modulus of the left wheels. Denote the rolling resistance of the left wheels as $f_{l.r}$. The input torque τ_l of the left motor equals the resistance torque of the left wheel $\tau_{l.Res}$, such that

$$\tau_l = \tau_{l.Res} = r(F_{l.f} + f_{l.r}). \quad (21)$$

Using (19) and the left equation of (21) with (6) yields

$$C(q, \dot{q}) = [\tau_{l.Res} \ \tau_{r.Res}]^T. \quad (22)$$

Substituting (5), (22) and $G(q) = 0$ into (4) yields a dynamic model that can be used to predict 2D movement for the skid-steered vehicle:

$$\begin{bmatrix} \frac{mr^2}{4} + \frac{r^2 I}{\alpha \beta^2} & \frac{mr^2}{4} - \frac{r^2 I}{\alpha \beta^2} \\ \frac{mr^2}{4} - \frac{r^2 I}{\alpha \beta^2} & \frac{mr^2}{4} + \frac{r^2 I}{\alpha \beta^2} \end{bmatrix} \ddot{q} + \begin{bmatrix} \tau_{l.Res} \\ \tau_{r.Res} \end{bmatrix} = \begin{bmatrix} \tau_l \\ \tau_r \end{bmatrix}. \quad (23)$$

In summary, in order to obtain (22), the shear displacement calculation of (12), (13), (15) and (16) is the first step. The inputs to these equations are the left and right wheel angular velocities ω_l and ω_r . The shear displacements are employed in (17) and (20) to obtain the right and left sliding friction forces, $F_{r.f}$ and $F_{l.f}$. Next, the sliding friction forces and rolling resistances are substituted into (18) and (21) to calculate the right and left resistance torques, which determine $C(q, \dot{q})$ using (22).

B. 3D Linear Motion

For 3D linear motion each wheel of the skid-steered vehicle can be assumed to be in pure rolling. The $F_{r.f}$ in (18) and $F_{l.f}$ in (21) are zero. Fig. 2 is the free body diagram of a skid-steered wheeled vehicle for this case. It is assumed that the surface elevation is described by $Z = f(Y)$ such that the left and right front wheels experience the same elevation and likewise for the rear wheels. (However, the below analysis can be extended to the more general case.) Let β denote the angle between the global coordinate axis Y and the body-fixed axis y_r (which can be determined analytically from $Z = f(Y)$), W the weight of vehicle, $f_{r.r}$ the rolling resistance of the right wheels, and F_r the traction force that acts on the vehicle. The left wheel forces are identical to those of the right wheels and are not shown in Fig. 2.

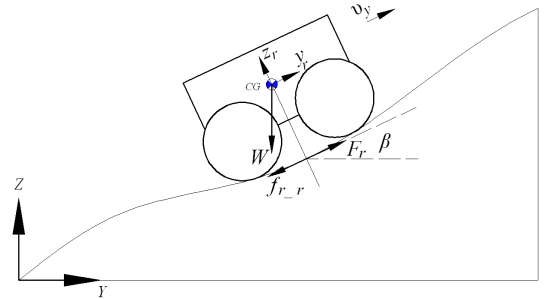


Fig. 2. Free-body diagram for vehicle hill climbing
The gravitational term $G(q)$ is generally nonzero and is given by

$$G(q) = \frac{mgr \sin \beta}{2} [1 \ 1]^T. \quad (24)$$

Substituting (5), (22) and (24) into (4) yields a dynamic model that can be used to predict 3D motion, given the assumption $Z = f(Y)$:

$$\begin{bmatrix} \frac{mr^2}{4} + \frac{r^2 I}{\alpha B^2} & \frac{mr^2}{4} - \frac{r^2 I}{\alpha B^2} \\ \frac{mr^2}{4} - \frac{r^2 I}{\alpha B^2} & \frac{mr^2}{4} + \frac{r^2 I}{\alpha B^2} \end{bmatrix} \ddot{q} + \begin{bmatrix} \tau_{l_Res} \\ \tau_{r_Res} \end{bmatrix} + \begin{bmatrix} \frac{mgr \sin \beta}{2} \\ \frac{mgr \sin \beta}{2} \end{bmatrix} = \begin{bmatrix} \tau_l \\ \tau_r \end{bmatrix}. \quad (25)$$

For the experimental verification in Section V, β is constant since the experiments were performed on surfaces with constant slopes.

IV. CLOSED-LOOP CONTROL SYSTEM

The dynamic models described above are essential parts of simulation models used to predict the vehicle motion. However, no matter how detailed the analysis, these models will have uncertain parameters, e.g., the coefficient of rolling resistance, coefficient of friction and shear modulus.

The models of open-loop and closed-loop control systems that can be utilized to predict motion are shown in Fig. 3 for one side of the vehicle. The complete control system for the vehicle is the combination of the two control systems for each side of the vehicle. The open-loop system consists of four parts: vehicle dynamics, terrain interaction, motor and motor controller. The closed-loop control system additionally includes the PID speed controller for the motor in a unity feedback. As is experimentally illustrated in Fig. 10 of Section V, the open-loop system is highly sensitive to these uncertainties and hence can yield poor velocity predictions, while the feedback system can dramatically reduce the effects of the model uncertainty. In most of the experimental results described in the next section, the closed-loop model is employed as the simulation model.

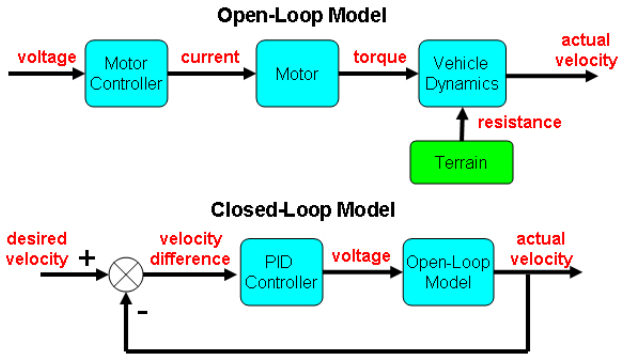


Fig. 3. The open-loop and closed-loop control systems for the left or right side of a skid-steered wheeled vehicle.

The vehicle dynamics and terrain-vehicle interaction were described in Section III. The remaining three parts, the PID controller, motor and motor controller, are described below.

In our research, a modified PID controller, for which the input to the derivative term is the reference signal, not the error signal, was adopted from [13]. The PID parameters are tuned by following the rules in Chapter 9 of [13].

We assumed the moment of inertia and viscous friction of the motor are small compared to the moment of inertia and

friction associated with the vehicle, so the dynamics of the motor have been neglected. However, we included the speed vs. current curve for a DC motor [14], which is of the form $\omega_m = -\eta I_m + b(V_m)$, where ω_m and I_m are respectively the angular velocity and current of the motor, $\eta > 0$ such that the slope is negative, and $b(V_m)$ changes monotonically with the motor voltage V_m . The motor must be constrained such that $I_m < I_{max}$, where I_{max} represents the maximum current allowable before the motor is in danger of overheating and burning out; this current constraint yields a safe region under the speed vs. current curve.

The motor controller can be viewed as an electrical drive system for the motor. The Maxon 4-Q-DC motor controller has been utilized in this research and has a maximum output voltage $V_{m,max}$, which has been modeled as a saturation constraint.

V. EXPERIMENTAL VERIFICATION

This section describes parts of the experiments that have been conducted to verify the closed-loop control system, including the PID controller, motor controller, motor, vehicle dynamics and terrain interaction. The model was simulated in SIMULINK to provide the theoretical results, which were compared with the experimental results.

The experimental platform is the modified Pioneer 3-AT shown in Fig. 4. The original, nontransparent, speed controller from the company was replaced by a PID controller and motor controller. PC104 boards replaced the original control system boards that came with the vehicle. Two current sensors were mounted on each side of the vehicle to provide real time measurement of the motors' currents.



Fig. 4. Modified Pioneer 3-AT entering a white-board ramp

Let μ_{sa} denote the coefficient of friction for the wheels when the current and angular velocity of the motor have the same sign such that the motor applies a propulsive force. Let μ_{op} denote the coefficient of friction for a wheel when the two have the opposite sign, resulting in the motor applying a braking force. The values of the parameters K , μ_{sa} and μ_{op} are terrain dependent and are difficult to determine by direct measurement. As a result, the values of K , μ_{sa} and μ_{op} are computed by solving the non-linear optimization problem,

$$\min_{K, \mu_{sa}, \mu_{op}} \sum_{i=1}^N [(\Delta \tau_{l_Res}^{(i)})^2 + (\Delta \tau_{r_Res}^{(i)})^2], \quad (26)$$

where i denotes the i^{th} of N experiments and $\Delta \tau_{l_Res}^{(i)}$ and $\Delta \tau_{r_Res}^{(i)}$ are the values of the difference between

TABLE I
 K , μ_{sa} AND μ_{op} FOR DIFFERENT N

N	K	μ_{sa}	μ_{op}	N	K	μ_{sa}	μ_{op}
2	0.00060	0.4609	0.3186	7	0.00054	0.4437	0.3093
3	0.00051	0.4567	0.3193	8	0.00056	0.4321	0.3033
4	0.00064	0.4521	0.3113	11	0.00054	0.4323	0.3061
5	0.00061	0.4510	0.3109	16	0.00052	0.4208	0.2981
6	0.00059	0.4400	0.3083	31	0.00050	0.4151	0.2964

TABLE II
PARAMETERS FOR CLOSED-LOOP SYSTEM MODEL

Vehicle		
Mass (kg)	m	30.6
Width of vehicle (m)	B	0.40
Width of wheel (m)	b	0.05
Length of L (m)	L	0.31
Length of C (m)	C	0.24
Radius of tire (m)	r	0.1075
PID Controller		
Proportional value	K_p	30.25
Integral value	K_i	151.25
Derivative value	K_d	0.0605
Motor		
Stall torque (Nm)	τ_s	0.2775
No-load speed (rad/s)	ω_n	487.16
Nominal voltage (V)	V_{nom}	12
Max Continuous Current (A)	I_{max}	5.5
Torque constant	K_T	0.023
Gear ratio	g_r	49.8
Motor Controller		
Pulse-width modulation	PWM	0.95
Vinyl Lab Surface		
Expansion factor	α	1.5
Shear deformation modulus (m)	K	0.00054
Coefficient of rolling resistance	$\mu_{roll,lab}$	0.0371
Coefficient of friction, of μ_{sa}	μ_{sa}	0.4437
Coefficient of friction, of μ_{op}	μ_{op}	0.3093
Asphalt Surface		
Coefficient of rolling resistance	$\mu_{roll,asphalt}$	0.051

the steady-state simulation and experimental torques. The commanded turning radius R is defined as the turning radius resulting from applying the wheel speeds, ω_l and ω_r , to the kinematic model (2) assuming no slip. The set of experimental indices i given by $\{1, 2, \dots, 31\}$ map to the set of commanded turning radii R given by $\{0.2, 0.3, \dots, 1, 2, \dots, 10^1, 10^{1.2}, \dots, 10^2, 10^{2.2}, \dots, 10^{3.2}, 10^{3.6}, 10^4\}$. The optimal K , μ_{sa} and μ_{op} for various values of $N \in \{2, 3, \dots, 31\}$ were found using the MATLAB Optimization Toolbox function `lsqnonlin` and are given in Table I. For each N the corresponding i were chosen to be evenly spaced. Although as N increases, Table I shows that the values of these parameters do appear to converge, the variation from $N = 2$ to $N = 31$ is modest (16.7% for K , 9.9% for μ_{sa} , and 7.0% for μ_{op}). Hence, these results show that only a small number of experiments are needed to determine the coefficients of friction and shear moduli. All of the key parameters for the model of the closed-loop system are listed in Table II.

A. 2D Circular Movement

In this subsection, 2D circular motion results are presented. When a skid-steered wheeled vehicle is in constant velocity circular motion, the left and right wheel torques are governed respectively by (21) and (18). The theoretical and experimental torques for different commanded radii are

shown in Fig. 5. If shear stress is not a function of shear displacement, but instead takes on a maximum value when there is a small relative movement between wheel and terrain, the left and right motor torques should be constant for different commanded turning radii, a phenomenon not seen in Fig. 5. Instead this figure shows the magnitudes of both the left and right torques reduce as the commanded turning radius increases. The same trend is found in [10], [11].

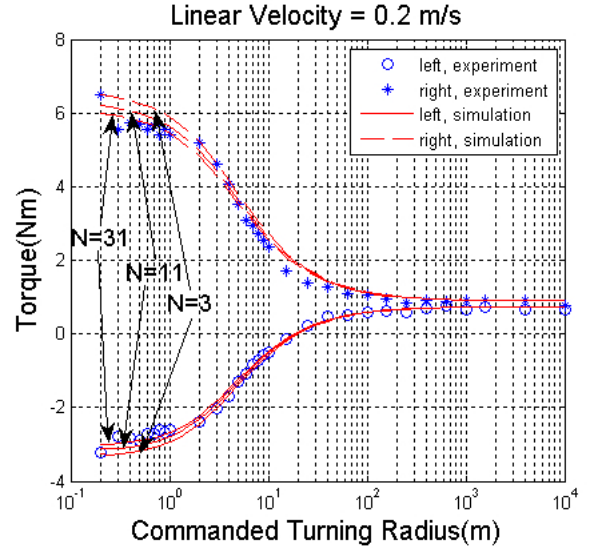


Fig. 5. Vehicle left and right wheel torque comparison during steady-state CCW rotation for different commanded turning radii on the lab vinyl surface.

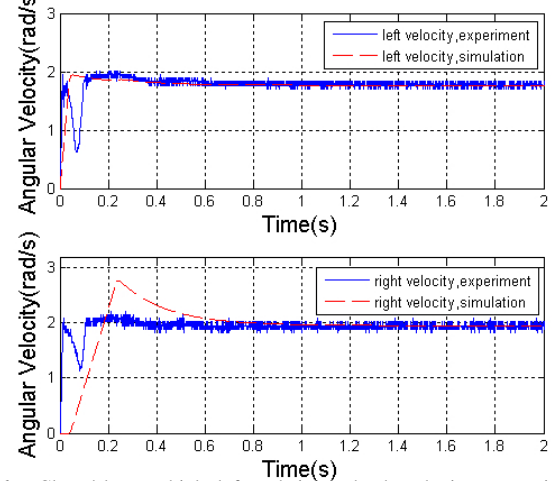


Fig. 6. Closed-loop vehicle left and right wheels velocity comparison for 2D circular movement on the lab vinyl surface

The extreme case is that when the vehicle is in straight-line movement, the sliding friction is zero, and the motor torque only has to compensate for the rolling resistance torque. It should be mentioned that if the load transfer from the left wheel to the right wheel is not large, experimental results have shown that the steady-state torques of the left and right wheels for different commanded turning radii are nearly the same for commanded linear velocities from 0.1 m/s to 0.6m/s, which is modeled accurately by (21) and (18).

Fig. 6 and Fig. 7 show the results when the vehicle is commanded to rotate at a constant velocity, beginning from a zero initial velocity. The commanded linear velocity and

commanded radius to the vehicle are 0.2 m/s and 4m on the lab vinyl surface. Note that there is some mismatch between the experimental and simulation velocities during the acceleration phase of the motion ($< 1s$). This is not surprising since constant velocity was assumed in the development of the resistance term $C(q, \dot{q})$. Therefore, if the vehicle has significant acceleration for a long time during rotation, the prediction becomes increasingly inaccurate. It should be noted that our current models are fairly precise in taking into account the influence of acceleration through the mass matrix (i.e., by $M\dot{q}$), which allows them to accurately describe acceleration when moving linearly and take into account some of the influence of acceleration when turning.

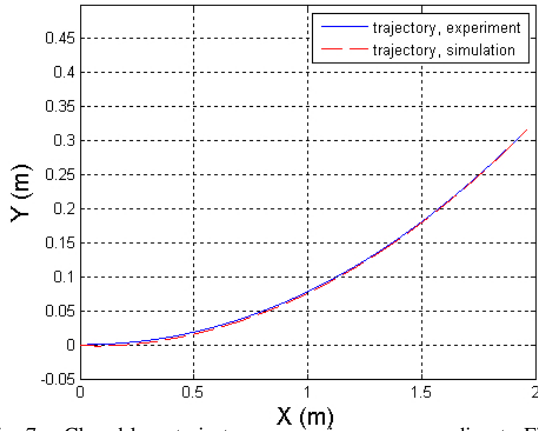


Fig. 7. Closed-loop trajectory comparison corresponding to Fig. 6

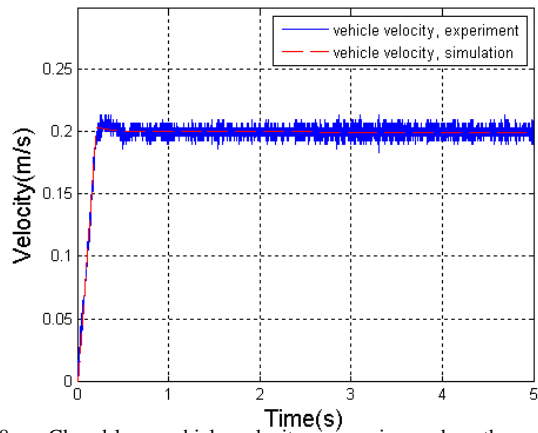


Fig. 8. Closed-loop vehicle velocity comparison when the vehicle is commanded to 0.2 m/s for straight-line movement on the lab vinyl surface

B. 2D and 3D Linear Movement

Fig. 8, Fig. 9 and Fig. 10 show comparisons of both open-loop and closed-loop experimental and simulation results for linear 2D motion. The vehicle is commanded at an acceleration of 1 m/s^2 to a velocity of 0.2 m/s for straight-line movement on the lab vinyl surface. Fig. 10 uses the experimental torque of Fig. 9 as the system input. It is seen that the closed-loop system gives a much better prediction of the vehicle velocity than the open-loop system.

Fig. 11 shows the velocity comparison of closed-loop experimental and simulation results for linear 2D motion when the vehicle is commanded to an unachievable velocity of 1.5 m/s. From Fig. 11, it can be seen that due to the saturation and power limitation of actuators, the vehicle can

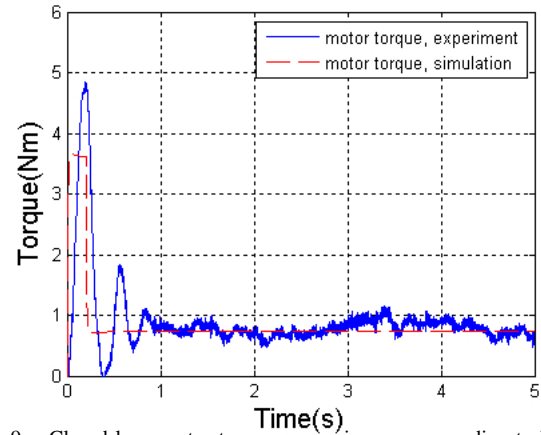


Fig. 9. Closed-loop motor torque comparison corresponding to Fig. 8

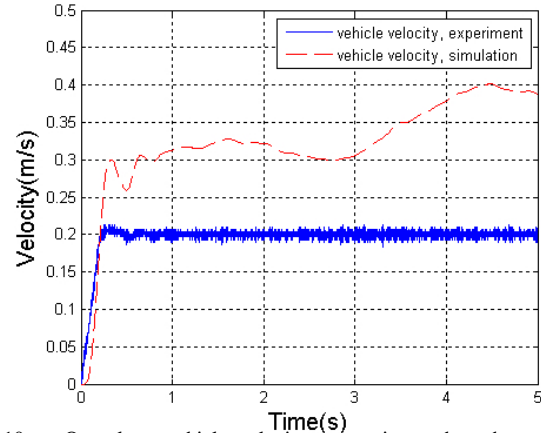


Fig. 10. Open-loop vehicle velocity comparison when the vehicle is commanded at the same torque of Fig. 9

only reach the final velocity of around 0.93 m/s, but not the desired 1.5 m/s.

Fig. 12, Fig. 13, and Fig. 14 illustrate hill-climbing for these 3 cases: (a) the ability to traverse a ramp at the commanded velocity, (b) the ability to traverse a ramp that is so steep that the vehicle decelerates while climbing no matter what the commanded velocity, and (c) the inability to traverse a steep ramp because of inadequate initial velocity. These results clearly demonstrate the ability of the model to predict traversal times on undulating terrains and to predict the inability of the vehicle to traverse a steep hill.

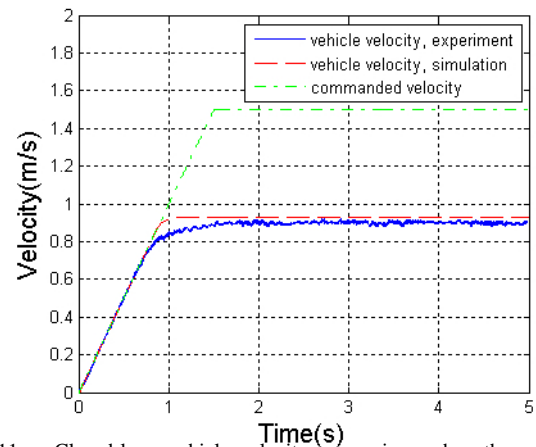


Fig. 11. Closed-loop vehicle velocity comparison when the vehicle is commanded to 1.5 m/s for straight-line movement on the lab vinyl surface

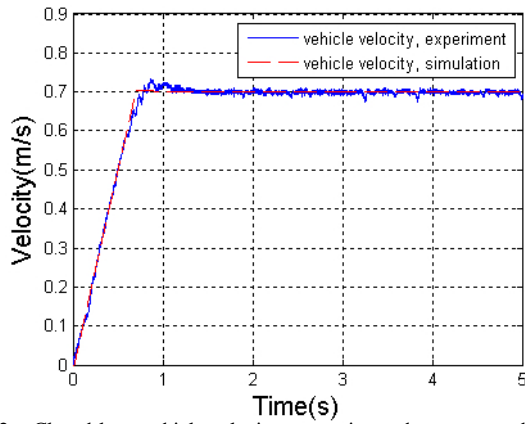


Fig. 12. Closed-loop vehicle velocity comparison when commanded linear velocity=0.7 m/s for asphalt hill climbing with slope $\beta = 5.4^\circ$

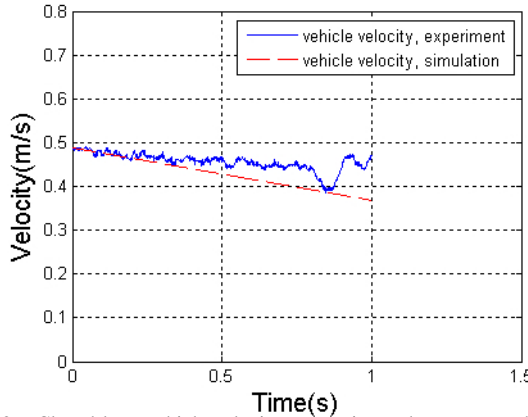


Fig. 13. Closed-loop vehicle velocity comparison when commanded linear velocity=1.2 m/s with 0.49m/s initial velocity for wood-board hill climbing with slope $\beta = 15.0^\circ$

VI. CONCLUSION

This paper developed dynamic models for skid-steered wheeled vehicles for general 2D motion and linear 3D motion. Unlike most previous research these models were developed assuming a specific functional relationship between the shear stress and shear displacement. This research also considers the acceleration and gravitational terms in addition to taking into account the PID controller, the motor and motor controller. An important contribution of this research is its focus on the closed-loop dynamics, which enable more accurate predictions of the vehicle velocity than that achievable with an open-loop model. The dynamic models are validated using extensive experimentation and seen to yield accurate

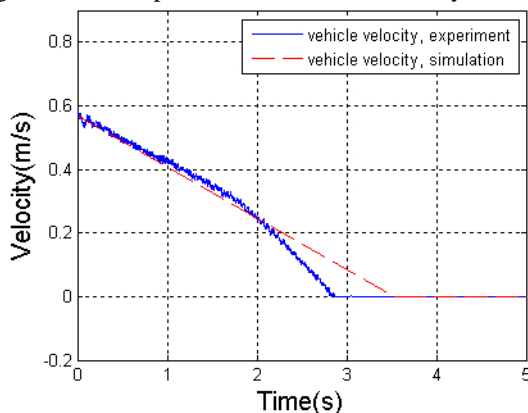


Fig. 14. Closed-loop vehicle velocity comparison when commanded linear velocity=1.2 m/s with 0.57m/s initial velocity for white-board hill climbing with slope $\beta = 13.5^\circ$

predictions of velocity and reasonable predictions of torque.

One limitation of the research is that the resistance term was developed using a constant velocity assumption and hence, although the models tend to give good results for linear motion in which the wheels are in pure rotation, they tend to lead to prediction inaccuracies when the vehicle is accelerating while turning. Another limitation is that no model was developed for general 3D motion.

Future research will develop a model for general 3D motion and seek models that are valid when the vehicle is accelerating in turns. In addition, the models will be used for motion planning, including energy efficient motion planning.

VII. ACKNOWLEDGEMENTS

Prepared through collaborative participation in the Robotics Consortium sponsored by the U. S. Army Research Laboratory under the Collaborative Technology Alliance Program, Cooperative Agreement DAAD 19-01-2-0012. The U. S. Government is authorized to reproduce and distribute reprints for Government purposes notwithstanding any copyright notation thereon.

REFERENCES

- [1] Roland Siegwart and Illah R. Nourbakhsh. *Introduction to Mobile Robotics*. MIT Press, Cambridge, MA, 2005.
- [2] Anthony Mandow, Jorge L. Martinez, Jess Morales, Jose-Luis Blanco, Alfonso Garcia-Cerezo, and Javier Gonzalez. Experimental kinematics for wheeled skid-steer mobile robots. In *Proceedings of the International Conference on Intelligent Robots and Systems*, pp. 1222–1227, San Diego, CA, 2007.
- [3] Luca Caracciolo, Alessandro De Luca, and Stefano Iannitti. Trajectory tracking control of a four-wheel differentially driven mobile robot. In *Proceedings of the International Conference on Robotics and Automation*, pp. 2632–2638, Detroit, MI, May 1999.
- [4] Krzysztof Kozłowski and Dariusz Pazderski. Modeling and control of a 4-wheel skid-steering mobile robot. *International Journal of Mathematics and Computer Science*, pp. 477–496, 2004.
- [5] Jingang Yi, Junjie Zhang, Dezhen Song, and Suhada Jayasuriya. IMU-based localization and slip estimation for skid-steered mobile robot. In *Proceedings of the International Conference on Intelligent Robots and Systems*, pp. 2845–2849, San Diego, CA, 2007.
- [6] Zibin Song, Yahya H Zweiri, and Lakmal D Seneviratne. Non-linear observer for slip estimation of skid-steering vehicles. In *Proceedings of the International Conference on Robotics and Automation*, pp. 1499–1504, Orlando, FL, May 2006.
- [7] Jingang Yi, Dezhen Song, Junjie Zhang, and Zane Goodwin. Adaptive trajectory tracking control of skid-steered mobile robots. In *Proceedings of the International Conference on Robotics and Automation*, pp. 2605–2610, Roma, Italy, April 2007.
- [8] Oscar Chuy Jr., Emmanuel G. Collins Jr., Wei Yu, and Camilo Ordonez. Power modeling of a skid steered wheeled robotic ground vehicle. In *Proceedings of the International Conference on Robotics and Automation*, pp. 4118–4123, Kobe, Japan, May 2009.
- [9] J.L. Martinez, A. Mandow, J. Morales, S. Pedraza, and A. Garcia-Cerezo. Approximating kinematics for tracked mobile robots. *International Journal of Robotics Research*, pp. 867–878, 2005.
- [10] J. Y. Wong. *Theory of Ground Vehicles*. John Wiley & Sons, Inc, 3rd edition, 2001.
- [11] J. Y. Wong and C. F Chiang. A general theory for skid steering of tracked vehicles on firm ground. *Proceedings of the Institution of Mechanical Engineers, Part D, Journal of Automotive Engineering*, pp. 343–355, 2001.
- [12] J. Morales, J. L. Martinez, A. Mandow, A. Garcia-Cerezo, J. Gomez-Gabriel, and S. Pedraza. Power analysis for a skid-steered tracked mobile robot. *Proceeding of the International Conference on Mechatronics*, pp. 420–425, 2006.
- [13] John J. Craig. *Introduction to Robotics: Mechanics and Control*. Prentice Hall, 3rd edition, 2004.
- [14] Giorgio Rizzoni. *Principles and Applications of Electrical Engineering*. McGraw-Hill, 2000.